Efficient PAW-Based Bond Strength Analysis for Understanding the In/Si(111)(8 × 2) – (4 × 1) Phase Transition

Andreas Lücke ,*[a] Uwe Gerstmann,[a] Thomas D. Kühne,[b] and Wolf G. Schmidt[a]

A numerically efficient yet highly accurate implementation of the crystal orbital Hamilton population (COHP) scheme for plane-wave calculations is presented. It is based on the projector-augmented wave (PAW) formalism in combination with norm-conserving pseudopotentials and allows to extract chemical interactions between atoms from band-structure calculations even for large and complex systems. The potential of the present COHP implementation is demonstrated by an in-depth analysis of the intensively investigated metal-insulator transition in atomic-scale indium wires self-assembled on the Si(111) surface. Thereby bond formation between In atoms of adjacent zigzag chains is found to be instrumental for the phase change. © 2017 Wiley Periodicals, Inc.

DOI: 10.1002/jcc.24878

Introduction

Many condensed-matter quantum-mechanical codes use plane waves (PWs) for the representation of the wave functions. They allow for an efficient and reliable control of the numerical convergence and do not suffer from the basis set superposition error that occurs for bases formed from a finite number of localized atom-centered functions. Thereby PWs are naturally suited to describe systems with periodic boundary conditions. However, they are delocalized by their very nature and, thus, do not give immediate access to electron partitioning and bonding information, which is more straightforwardly obtained from an atomic/molecular orbital description of the electronic structure.[1–5] To gain such information from PW calculations, projection techniques have to be applied.[6–13]

The crystal orbital Hamilton population (COHP) analysis, proposed by Dronskowski and Blöchl,[3] uses a Linear Muffin-Tin Orbital approach and is a very successful bonding indicator for extended structures. Thereby the band-structure energy is rewritten as a sum of orbital pair contributions. The energy dependent COHP(E) diagram allows for identifying bonding, nonbonding, and antibonding regions within a specified energy range. The energy integral of COHP(E) gives access to the contribution of an atom or a chemical bond to the distribution of one-particle energies and indicates the total bond strength (ICOHP). Maintz et al.[11–13] recently proposed a scheme to calculate COHP diagrams within a PW framework using Blöchl's projector-augmented wave (PAW) method.[14] The present study is a follow-up to the implementation suggested in Refs. [11–13]. Here, it is shown that a remarkable further substantial speedup in the COHP calculation can be achieved by making use of a rigorous application of the PAW formalism and simplifications coming with norm-conserving pseudopotentials.[15–17] This improvement allows for applying the COHP bonding indicator to larger and more complex structures than addressed previously.

The In/Si(111) (8 × 2) → (4 × 1) phase transition[18] is used to demonstrate the prowess of the COHP approach. The mechanism and driving force for this phase transition has been controversially discussed since it's discovery. In particular, it is presently discussed whether the phase transition is of order-disorder[19] or displacive type,[20] and whether it can be characterized as Peierls transition[21] or should rather be addressed as an exothermic reaction with the consecutive bond-breaking and bond-making processes.[22] The investigation of these questions will certainly profit from a quantitative investigation of the relevant bond strengths. This holds as well for the question by which mechanisms the phase transition can be optically triggered.[23–25]

In this manuscript, we first outline the fast projection scheme proposed by the present authors and its parallel implementation. Then, a comparison is made with the implementation proposed by Maintz et al.,[11–13] where our work is based on, and it is shown that both approaches lead to identical results. Finally, we apply the COHP formalism to the In/Si(111) surface and show in detail how the insulator-metal transition is related to changes of characteristic bond strengths.

Methodology

According to Blöchl,[3] COHP is formally defined as

[a] A. Lücke, U. Gerstmann, W. G. Schmidt
Lehrstuhl für Theoretische Materialphysik, Universität Paderborn, Paderborn 33095, Germany
E-mail: ALuecke@gmx.net
[b] T. D. Kühne
Lehrstuhl für Technische Chemie, Universität Paderborn, Paderborn, 33095, Germany

Contract grant sponsor: The Deutsche Forschungsgemeinschaft; Contract grant numbers: FOR1700 and SPP1601

$$\mathrm{COHP}_{\mu\vec{T},\nu\vec{T}'}(E) = H_{\mu\vec{T},\nu\vec{T}'}\sum_{j,\vec{k}} f_j(\vec{k})C^{*}_{\mu\vec{T},j}(\vec{k})C_{\nu\vec{T}',j}(\vec{k})\delta(\varepsilon_j(\vec{k})-E) \quad (1)$$

Here, $C_{\mu\vec{T},j}(\vec{k})$ is the expansion coefficient of the jth band at k-point $\vec{k}$ in terms of the atomic orbital μ at the atomic position $\vec{T}$. $H_{\mu\vec{T},\nu\vec{T}'}$ denotes the matrix elements of the Hamiltonian in atomic orbitals, $\varepsilon_j(\vec{k})$ is the eigenvalue corresponding to the jth electron state and $f_j(\vec{k})$ its occupation number. The off-site COHP (for $\vec{T} \neq \vec{T}'$) frequently serves as bonding indicator in extendend systems.[3,10,11] Thereby the occupation number may be omitted, for example, for characterizing the bonding character of conduction states.

In case of PW calculations, the expansion coefficients $C_{\mu\vec{T},j}(\vec{k})$ are determined by postprocessing the electronic structure, that is, by projecting the PWs on atomic orbitals. Maintz et al.[11] suggested to use Bloch sums[26] $\chi_\mu(\vec{k})$ setup from contracted multiple-ζ Slater-type orbitals as atomic basis onto which the all-electron (AE) wave functions $|\psi_j(\vec{k})\rangle$ are projected

$$T_{\mu j}(\vec{k}) = \langle\chi_\mu(\vec{k})|\psi_j(\vec{k})\rangle, \quad (2)$$

whereby the $T_{\mu j}(\vec{k})$ can be directly related to the expansion coefficients $C_{\mu\vec{T},j}(\vec{k})$ (cf., Ref. 11).

For the projection, the AE wave function $|\psi_j(\vec{k})\rangle = \mathcal{T}|\tilde{\psi}_j(\vec{k})\rangle$ is reconstructed from the PAW pseudo wave function $|\tilde{\psi}_j(\vec{k})\rangle$ using the transformation $\mathcal{T}$:

$$\mathcal{T} = 1 + \sum_{\mu,\vec{T}} \left(|\phi_{\mu\vec{T}}\rangle - |\tilde{\phi}_{\mu\vec{T}}\rangle\right)\langle\tilde{p}_{\mu\vec{T}}| \quad (3)$$

Here, $|\phi_{\mu\vec{T}}\rangle$ and $|\tilde{\phi}_{\mu\vec{T}}\rangle$ denote the AE and pseudo atomic partial waves, respectively and $\langle\tilde{p}_{\mu\vec{T}}|$ the projector function (cf., Ref. [27]). The atomic orbital projection formalism in Ref. [11] involves three distinct scalar products—indicated below—which have to be evaluated on different grids for accurate results

$$T_{\mu j}(\vec{k}) = \overbrace{\langle\chi_\mu(\vec{k})|\tilde{\psi}_j(\vec{k})\rangle}^{(1)} + \sum_{\mu,\vec{T}} \underbrace{\langle\chi_\mu(\vec{k})|\left(|\phi_{\mu\vec{T}}\rangle - |\tilde{\phi}_{\mu\vec{T}}\rangle\right)}_{(2)} \underbrace{\langle\tilde{p}_{\mu\vec{T}}|\tilde{\psi}_j(\vec{k})\rangle}_{(3)}. \quad (4)$$

To reduce the number of scalar products needed, we propose a different application of the PAW projection. Thereby we start from the atomic partial waves $|\phi_{\mu,\vec{T}}\rangle$ generated along with the PAW pseudopotential data and use these as localized basis to setup the Bloch sums[28]

$$|\chi_\mu(\vec{k})\rangle = \frac{1}{\sqrt{N_{\vec{T}}}}\sum_{\vec{T}} e^{i\vec{k}\vec{T}}|\phi_{\mu\vec{T}}\rangle. \quad (5)$$

This requires pseudopotentials with atomic wave functions generated on a sufficiently large radial grid (the standard used in the `Quantum Espresso` pseudopotential database is large enough). The use of the atomic partial waves $|\phi_{\mu\vec{T}}\rangle$ generated in conjunction with the PAW data in combination with norm-conserving pseudopotentials[15–17] allows for a considerable reduction of the computational effort as will be shown in the following.

Inserting eq. (5) into eq. (2) yields

$$\begin{aligned} T_{\mu j}(\vec{k}) &= \frac{1}{\sqrt{N_{\vec{T}}}}\sum_{\vec{T}} e^{-i\vec{k}\vec{T}}\langle\phi_{\mu\vec{T}}|\psi_j(\vec{k})\rangle \\ &= \frac{1}{\sqrt{N_{\vec{T}}}}\sum_{\vec{T}} e^{-i\vec{k}\vec{T}}\langle\tilde{\phi}_{\mu\vec{T}}|\mathcal{T}^{\dagger}\mathcal{T}|\tilde{\psi}_j(\vec{k})\rangle, \end{aligned} \quad (6)$$

where the $\mathcal{T}^{\dagger}\mathcal{T}$ transformation can be expressed as

$$\mathcal{T}^{\dagger}\mathcal{T} = 1 + \sum_{\mu,\nu,\vec{T}} |\tilde{p}_{\mu\vec{T}}\rangle \underbrace{\left(\langle\phi_{\mu\vec{T}}|\phi_{\nu\vec{T}}\rangle - \langle\tilde{\phi}_{\mu\vec{T}}|\tilde{\phi}_{\nu\vec{T}}\rangle\right)}_{\Delta S_{\mu,\nu,\vec{T}}}\langle\tilde{p}_{\nu\vec{T}}|. \quad (7)$$

This reformulation allows for evaluating eq. (6) solely on the Fourier grid using the pseudopotential specific constants $\Delta S_{\mu,\nu,\vec{T}}$, the pseudo wave functions $|\tilde{\psi}_j(\vec{k})\rangle$ and the projector functions $|\tilde{p}_{\mu\vec{T}}\rangle$. In other words, the whole projection scheme is exclusively based on information included in the pseudopotentials. Now, a drastic speedup can be gained using norm-conserving PAW pseudopotentials for which the atomic partial waves $\{|\phi_{\mu\vec{T}}\rangle\}$ and $\{|\tilde{\phi}_{\mu\vec{T}}\rangle\}$ can be chosen orthonormal so that $\Delta S_{\mu,\nu,\vec{T}}$ vanishes. This reduces the projection to a single scalar product of the pseudo partial wave $|\tilde{\phi}_{\mu\vec{T}}\rangle$ with the pseudo wave function $|\tilde{\psi}_j(\vec{k})\rangle$. Therefore, the sums over the projector functions become obsolete, hence an increasing number of scalar products with growing system size can be saved. This property of norm-conserving pseudopotentials reduced the overall runtime of our present COHP implementation by about 90% for the In/Si(111) system* compared to non norm-conserving pseudopotentials.

Technical implementation

The methodology described above has been implemented as post-processing tool for the Quantum Espresso-package,[29] see applications flow chart in Figure 1. Starting point—see first block in Figure 1—is the computation of Bloch sums from the atomic pseudo partial waves $|\tilde{\phi}_{\mu\vec{T}}\rangle$ which yields a k-dependent basis set. This set is orthonormalized in the next step, to use it for the determination of the expansion coefficients $\boldsymbol{C}(\vec{k})$. Thereby Löwdin's symmetric orthonormalization procedure is used, to limit the wave-function modifications to a minimum.[30] The Message Passing Interface is used to parallelize over PWs in the scalar products calculated in these first steps. The calculation of the coefficients $\boldsymbol{C}(\vec{k})$ has not been parallelized with respect to the k-points, as this leads to considerable random access memory for large systems.

However, once the $\boldsymbol{C}(\vec{k})$ are obtained, there are no PW dependent data to be processed anymore, and a parallelization with respect the **k** points is efficient and has been

*Presented in the results section

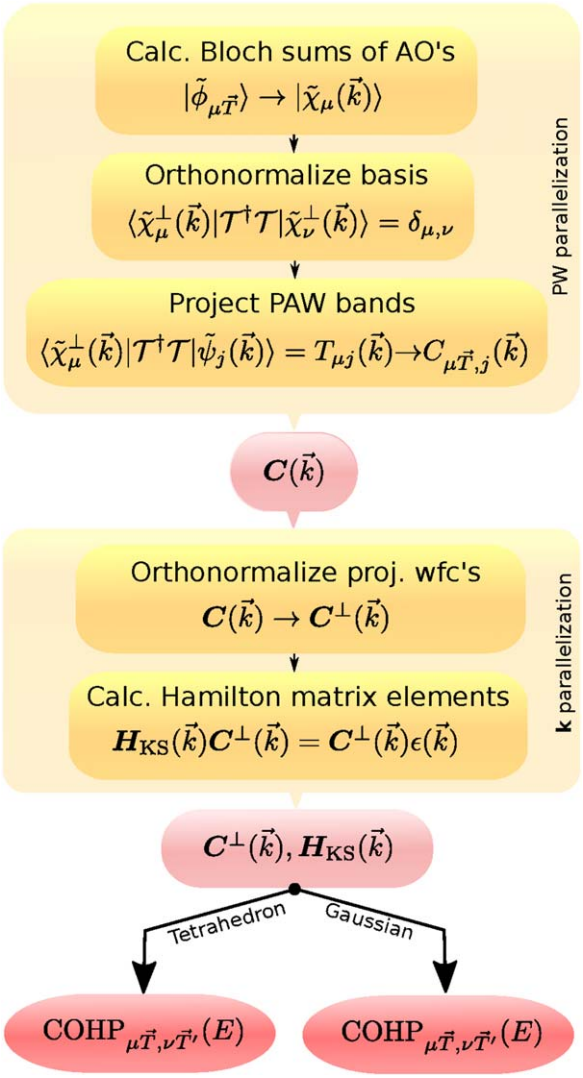

Figure 1. Flow chart for the calculation of COHP(E). Further details can be found in Refs. [11] and [13], with permission. [Color figure can be viewed at wileyonlinelibrary.com]

implemented. This concerns the re-orthonormalization of the projected wave function—the orthonormality of the PAW bands might be lost due to the projection—and the calculation of the Hamiltonian matrix elements $\boldsymbol{H}_{\mathrm{KS}}$ (cf., second block in Fig. 1). Here, $\varepsilon(\vec{k})$ denotes the Kohn-Sham eigenvalues from the density functional theory (DFT) electronic structure.

Finally, the COHP quantity can be determined by two ways: The tetrahedron method[14,31] offers a highly accurate way to visualize the results, but needs at least four **k** points. As an alternative, especially for molecules, a Gaussian broadening visualization was also implemented.

The present implementation and projection scheme was optimized in a way to offer best balance between speedup and memory consumption as the latter limits the number of parallel processes per node for large systems. Figure 2 shows a comparison of the computation times for the available implementation of the original projection scheme of Ref. [11] (LOBSTER) and our present implementation. As LOBSTER makes solely use of Open Multi-Processing (OpenMP) parallelization which is restricted to shared memory, we executed for the sake of comparability both implementations on a single node with 24 cores. The computation time is evaluated for the two systems to be discussed below, bulk diamond and indium nanowires on the Si(111) surface. Figure 2 shows that the present implementation is considerably faster than LOBSTER. Thereby it has to said the present approach is not restricted to shared memory, and therefore, a further speedup may be achieved using several nodes in parallel. Conversely, LOBSTER offers a broad range of options, for example, the possibility to calculate bond-weighted distribution functions or the crystal orbital overlap population, which are not implemented here.

How do the results obtained with the present implementation compare with the data obtained from the LOBSTER code? To answer this question, we perform COHP calculations for a simple and well defined model system, bulk diamond. The present calculations are based on the DFT electronic structure calculated using the Quantum Espresso package[29] within the generalized gradient approximation, specifically, using the PBE functional.[32,33] A PW basis up to an energy cutoff of 400 eV is used to expand the Kohn-Sham orbitals and the Brillouin zone is sampled with a 23 × 23 × 23 tetrahedron grid. The COHP diagram obtained here is compared with the data by Maintz et al.[11] in Figure 3. Negative and positive COHP values indicate bonding and antibonding contributions of electronic states within a specific energy interval. The occupied diamond valence states are thus clearcut bonding states (cf., Fig. 3), the conduction states above the band gap are antibonding in character. There is virtually no difference between the COHP values obtained with the present implementation compared to the LOBSTER data, resulting from a contracted multiple-ζ Slater-type orbitals basis set. This is confirmed by a small spilling value[6,11] of about 0.38% which is a good indicator for the quality of the projection.

Results

In/Si(111) (8 × 2) → (4 × 1) phase transition

The self-assembled In nanowires formed on annealing one monolayer indium on the Si(111) surface have long been investigated as model systems for electron transport at the

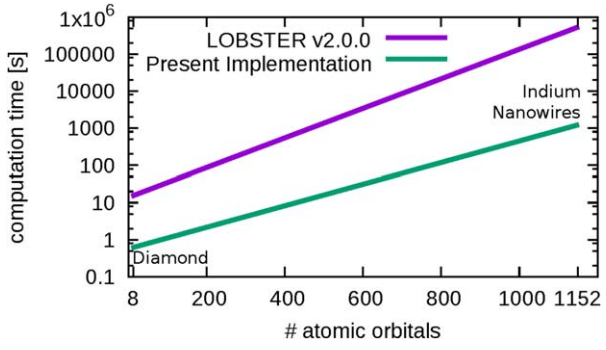

Figure 2. Wall clock time needed to calculate the COHP digram using LOBSTER and the present implementation for bulk diamond and In/Si(111) with 8 and 1152 atomic orbitals, respectively, (calculated on a single node with 24 cores). [Color figure can be viewed at wileyonlinelibrary.com]

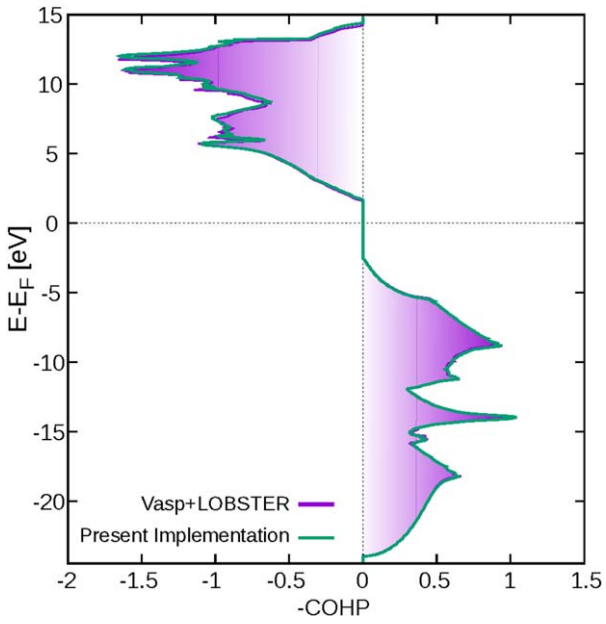

Figure 3. Comparison of the chemical bonding results for a C—C bond in diamond between Ref. [11] (purple, with permission) and the present implementation for the Quantum-espresso-package (green). Tetrahedron smearing is used in both cases to obtain smooth curves. [Color figure can be viewed at wileyonlinelibrary.com]

atomic scale and phase transitions in quasi one-dimensional structures.[18,20,34–41] The low-temperature semiconducting ground state of these nanowires is characterized by In hexagons arranged in a 8 × 2 translational symmetry.[19] Above about 120 K the In atoms arrange in metallic zigzag chains with 4 × 1 symmetry,[35] see Figure 4. Whether or not this insulator-metal transition can be classified as Peierls instability driven or not, and if it is a first- or second-order phase transition is controversially discussed up to now.[19,21,22]

Jeckelmann et al.[21] developed a simplified 1D lattice model for the In nanowire, where they focus on the bonds within outermost linear In chains and within a central In zigzag chain, as indicated in the bottom of Figure 4. These bonds couple most strongly to the soft In chain rotary and shear modes, the Peierls amplitude modes in In/Si(111). The reduction of the In bonding configuration to these bonds allows for decoupling the nanowire system into three independent chains with Su–Schrieffer–Heeger (SSH) Hamiltonians that suggest to interpret the 4 × 1 → 8 × 2 phase change as first-order grand canonical Peierls transition.[21] Kim and Cho,[22] conversely, stress the importance of bond-breaking and bond-making processes during the metal-insulator transition of the indium atom wires and classify the latter as an exothermic surface reaction.

The COHP analysis provides the possibility to determine the strength of specific In—In bonds within the complicated nanowire structure and to track quantitatively the bond strength changes during the phase transition. To that purpose, we perform DFT calculations within the local-density approximation for In/Si(111) surfaces modeled by three bilayers of Si with hydrogen termination at the bottom. We use 8 × 4 surface unit cells with 272 atoms, to avoid the double counting of bonds due to periodic image structures. Tetrahedron smearing with 16 **k** points is used to sample the surface Brillouin zone and PW basis with energy cutoff of 50 Ry is used to represent the electron orbitals. Norm-conserving PAW pseudopotentials[27] describe the electron-ion interaction. Thereby the In 4*d* electrons are treated as valence states. The calculated spilling value is about 0.26% which indicates again a good projection for the COHP calculation.

The COHP curves for two selected bonds are depicted in Figure 5, left. Integrating such curves along the energy axis (weighted with the occupation number) gives a measure for the bond strength (ICOHP). For several In—In bonds, these strengths are determined from the self-consistently calculated electronic structure of the In/Si(111) (4 × 1) and (8 × 2) phases and shown in Figure 5, right. It can be seen that the bonds in the 8 × 2 phase coincide well with the ones commonly assumed (cf., Fig. 4) forming the indium hexagons.

For the 4 × 1 phase the COHP analysis confirms the typical model of two regular outer zig-zag chains while there are nearly no outermost linear bonds in contrast to the tight binding fitting results of Ref. [21]. However, there are indeed strong bonds between the In atoms of the two zig-zag rows which are a substantial ingredient for the SSH Hamiltonian in Ref. [21], but have barely been discussed before.

The drastic bond strength changes calculated here between the 8 × 2 and the 4 × 1 phase, conversely, supports the more chemical interpretation of the phase transition in terms of bond-breaking and bond-formation.[22]

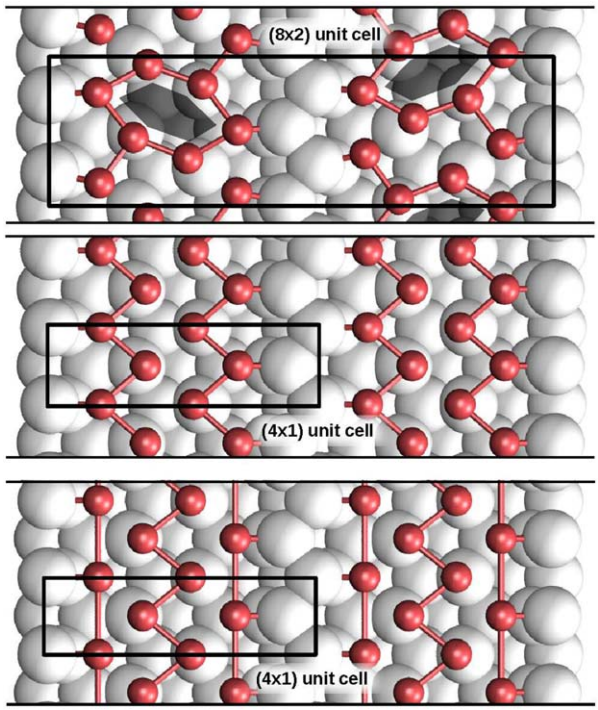

Figure 4. In/Si(111) surface models. Top: low temperature 8 × 2 phase ($T < 120$ K). Middle: room temperature 4 × 1 phase. Bottom: Different bonding model for the 4 × 1 high temperature phase assuming that the atoms form two linear chains surrounding one regular zig-zag chain. [Color figure can be viewed at wileyonlinelibrary.com]

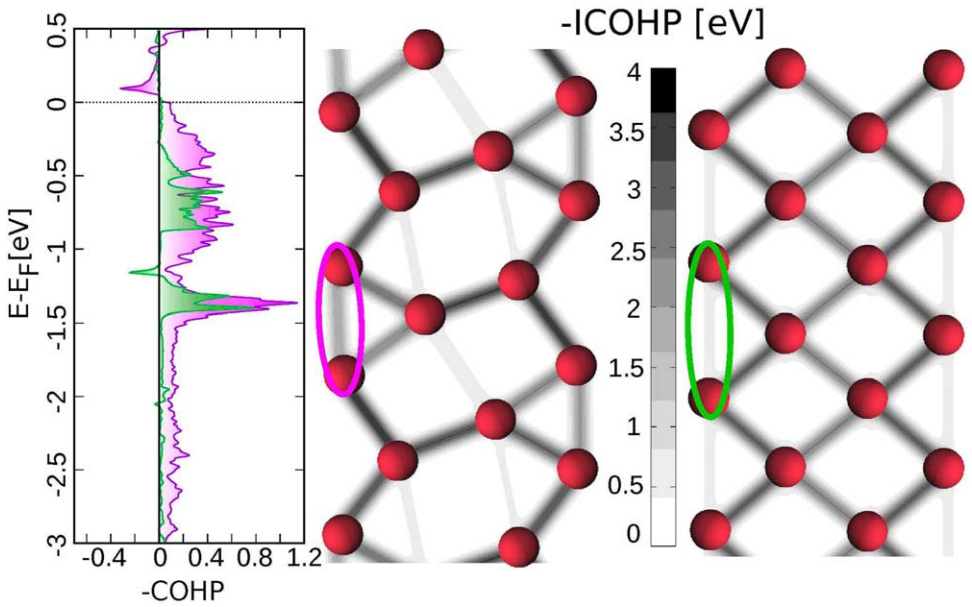

Figure 5. COHP analysis for the 8 × 2 and 4 × 1 phase. Left: COHP curves for two selected bonds marked on the right. Integrating such COHP curves weighted with the occupation number yields the total bond strength which is depicted as color code on the right (ICOHP). Dark drawn bonds indicate thereby the ones with largest bond strengths. [Color figure can be viewed at wileyonlinelibrary.com]

Do the bond strengths change abruptly or is this a rather smooth process during the phase transition? In Figure 6, the ICOHP bond strength of selected bonds is pursued along the generalized coordinate describing the 8 × 2 → 4 × 1 phase transition. Also shown in Figure 6 is the ground-state potential energy surface (PES), which shows a finite energy barrier between the two phases. The In—In bonds follow a monotonous behavior: There are bonds, most notable the ones indicated green and orange which are located diagonal to the In hexagons and strengthen considerably during the phase transition. Other bonds, in particular the bond indicated blue between outer-row In atoms clearly soften on the 4 × 1 phase formation. Interestingly, the bonds indicated green and blue in Figure 6 are exactly the bonds that couple most strongly to the shear and rotary phonon modes of the In/Si(111) surface.[20] These are the two Peierls lattice modes identified by Jeckelmann et al.[21] In all cases, we observe that the bond strengths change smoothly rather than abruptly during the phase transition.

As already mentioned above, the critical temperature T_c for the 8 × 2 → 4 × 1 phase transition is about 120 K.[18,20] However, Horn-von Hoegen and coorkers have shown that optical excitation, that is, a laser pulse with 1.5 eV photon energy may transform the 8 × 2 ground state into the 4 × 1 phase at temperatures considerably below T_c.[23,25] To rationalize this finding, we investigate in the following the influence of optically excited electron configurations on the In—In bond strengths.

A large variety of PESs for optically excited In/Si(111) surfaces were calculated using constrained DFT.[42] Thereby we excite electrons from the uppermost In valence states into the lowest In conduction states of the nanowire system, cf. calculated band structure in Figure 7.

Some excited-state PESs along the ground-state minimum energy path for the 8 × 2 → 4 × 1 transition are shown in Figure 8 in comparison to the ground-state PES. There are excitations, for example, the one indicated by the green line in Figure 8 that lower the relative energy difference between the 8 × 2 and 4 × 1 phases of the In/Si(111) surface, but do not quench the energy barrier separating the two phases. Such an energy curve is obtained, if the electrons at the Brillouin zone boundary are excited from valence to conduction states without momentum transfer, that is, across the small direct gap of the In/Si(111)(8 × 2) surface. If an additional momentum

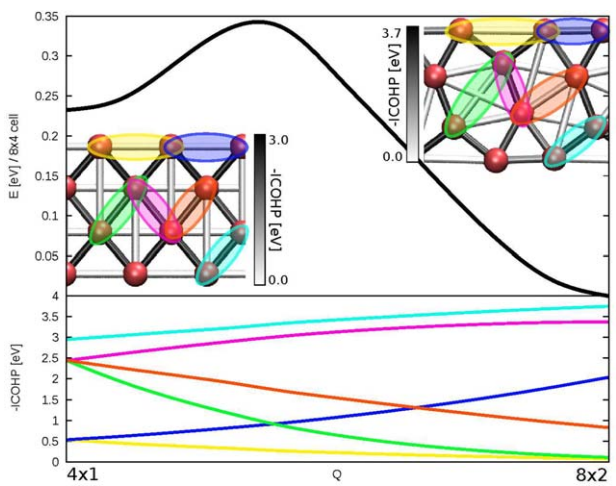

Figure 6. COHP bonding analysis between nearest neighbors for the two geometries. The darker a bond is drawn, the stronger it is. The black curve depicts the potential energy surface which exhibits two minima belonging to the 8 × 2 phase (right) and the 4 × 1 phase (left). The lower graph shows the bond strengths for six selected bonds along the phase transition. [Color figure can be viewed at wileyonlinelibrary.com]

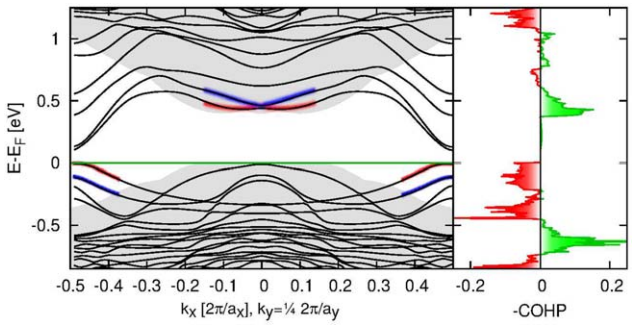

Figure 7. Left: Band structure of the 8 × 2 hexagon phase along the In wire. Grey areas correspond to the projected Si bulk states. Charge excitations involving the states marked blue and red are particularly effective for triggering the 8 × 2 – 4 × 1 phase transition, see text. Right: COHP diagram for the In—In bond marked green in Figure 6. [Color figure can be viewed at wileyonlinelibrary.com]

transfer occurs, and electrons from Brillouin zone boundary valence states are excited to zone center conductions states (see bands highlighted in Fig. 7) the 4 × 1 may even become more favorable than the 8 × 2 ground-state structure, as shown by the red and blue PESs in Figure 8. Moreover, the energy barrier separating the two geometrical structures vanishes and the energy is monotonously decreasing from 8 × 2 to 4 × 1. Such electronically excited configurations are obviously suitable to explain the laser-induced phase transition.[23,25] Can we understand the optically triggered phase transition in terms of modified bond strengths?

As discussed above, the In—In bonds across the zigzag chains (highlighted in green in Fig. 6) are strongly affected by the phase transition. They are strong in the 4 × 1 phase and barely effective in the 8 × 2 structure. The COHP diagram for these bonds is shown in Figure 7 rhs for the case of the 8 × 2 phase. It can be seen that valence and conduction band edge states have clear antibonding and bonding character, respectively. Electron excitation from the valence to the conduction states will thus strengthen these bonds, as observed for the 4 × 1 phase.

To understand the particular excitations from the bonding point of view, we analyzed the change in the bond strengths on excitation. The results are depicted in Figures 8a–8e where blue and red indicate an increase and decrease, respectively, in bond strength compared to the electronic ground state configuration. The bond strengthened most on excitation is marked in orange in Figures 6 and 8a. This bond is indeed far stronger for the 4 × 1 than the 8 × 2 phase, see Figures 5 and 6. The same holds also for the bond marked green in Figures 6 and 8a. This bond, however, gains more strength especially in intermediate configurations during the phase transition, cf., Figure 8d. Also in case of the bond weakening we can differentiate between bonds that lose most strength immediately on optical excitation, for example, the bond marked turquoise, and bonds that are affected especially at intermediate geometries, for example, the bond marked pink in Figures 8a and 8d. The bonds connecting the outer In chain atoms are also affected by electronic excitations. The bonds that are weaker in the 8 × 2 phase compared to the 4 × 1 structure, marked yellow in Figure 8a are strengthened, in particular if two electrons are excited, cf., Figure 8c. The electronic excitations from Brillouin zone boundary valence states and zone center conduction states thus affects exactly the bonds that increase in strength during the transition. These are also the bonds that enter the SSH Hamiltonians proposed in Ref. [21]. Moreover, the bonds opposite to the most strikingly green bond are severely weakened, making it more easier for the indium atoms to decrease the green bond length.

So far the bonding analysis has nicely illustrated why the excitations identified discussed above drive the phase transition. However, why do some excitations fail to drive the transition? Let us consider the occupation inversion at the Brillouin boundary (cf., green PES curve in Fig. 8). The COHP analysis shows a similar change in the bond strength compared to the one electron excitation discussed above (red curve in Fig. 8). For the 8 × 2 geometry, that is, at labels (a) and (b) in the respective PES, both excitations strengthen in particular the bonds marked orange in Figure 8a, that is, will initiate the phase change. This agrees with the nearly equal descent of the PESs at the beginning of the phase transition. However,

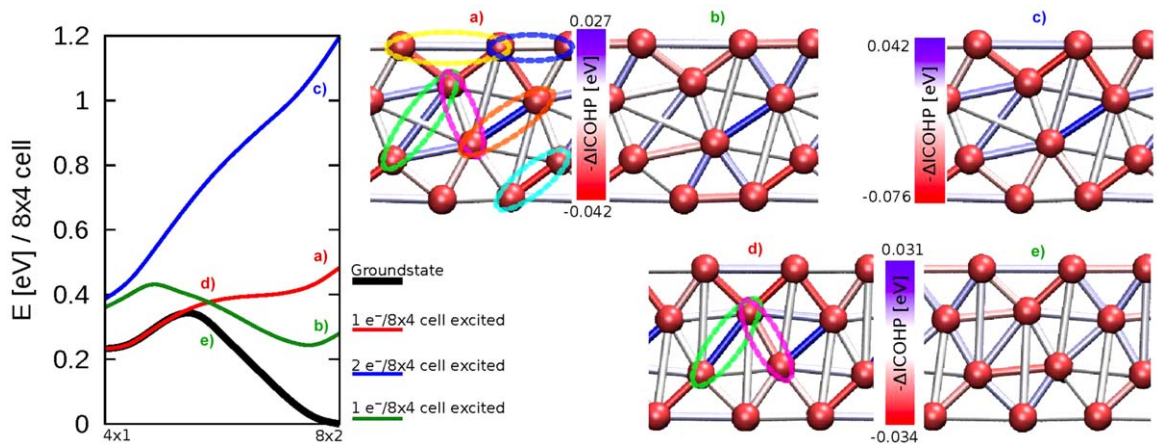

Figure 8. Left: Potential energy surfaces for the ground state (black), and for excitations of 1 (red) and 2 (blue) electrons per 8 × 4 unit cell involving the states marked in Figure 7. The dark green curve shows the PES for an occupation inversion at the direct band gap (Brillouin zone boundary). Right: ICOHP changes due to excitations indicated. Letters denote the respective position on the PES shown left. [Color figure can be viewed at wileyonlinelibrary.com]

the two electronic excitations differ in their influence on the bonds in an intermediate structure, that is, at labels (d) and (e). Here, the red PES continues to descent toward the 4 × 1 phase, while the green PES goes up in energy. This corresponds to the respective bond strength changes: The excitation involving Brillouin zone boundary and center states continues to strengthen the inner In-In zigzag chain bonds, which is clearly not the case for the excitation restricted to the zone boundary. Thus, the transition is not completed in the latter case.

Conclusions

An efficient PAW-based projection scheme for the calculation of the COHP has been proposed and implemented in the Quantum-espresso package. By projection on the atomic orbitals generated along with the PAW pseudopotentials, a significant speedup of the COHP calculations is possible. This allows to apply this scheme also to large system and complex scenarios. As an advanced prototype example, we explored the bond strengths at the In/Si(111)(8 × 2)/(4 × 1) surface, and their optically induced changes. Thereby we confirm that the bonds proposed recently for a SSH model of the surface[21] are indeed instrumental for the phase change. Conversely, taking advantage of the performance of the present approach, we find drastic bond strength changes on phase transition, in agreement with the interpretation recently proposed by Kim and Cho.[22]

Acknowledgments

We thank the Paderborn Center for Parallel Computing (PC²) and the Höchstleistungs-Rechenzentrum Stuttgart (HLRS) for grants of high-performance computer time. Atomic structure images were prepared using VMD[43] and the tachyon renderer. Furthermore, we thank Stefan Maintz for his support.

Keywords: density functional theory · bonding · crystal orbital Hamilton population · indium nanowires · phase transition

How to cite this article: A. Lücke, U. Gerstmann, T. D. Kühne, W. G. Schmidt. *J. Comput. Chem*. **2017**, *38*, 2276–2282. DOI: 10.1002/jcc.24878

[1] T. Hughbanks, R. Hoffmann, *J. Am. Chem. Soc.* **1983**, *105*, 3528.
[2] G. J. Miller, *Angew. Chem.* **1989**, *101*, 1570.
[3] R. Dronskowski, P. E. Blöchl, *J. Phys. Chem.* **1993**, *97*, 8617.
[4] A. Grechnev, R. Ahuja, O. Eriksson, *J. Phys.: Condens. Matter* **2003**, *15*, 7751.
[5] R. Z. Khaliullin, T. D. Kühne, *Phys. Chem. Chem. Phys.* **2013**, *15*, 15746.
[6] D. Sanchez-Portal, E. Artacho, J. M. Soler, *Solid State Commun.* **1995**, *95*, 685. ISSN 00381098.
[7] D. Sánchez-Portal, E. Artacho, J. M. Soler, *J. Phys.: Condens. Matter* **1996**, *8*, 3859.
[8] M. D. Segall, C. J. Pickard, R. Shah, M. C. Payne, *Mol. Phys.* **1996**, *89*, 571.
[9] M. D. Segall, R. Shah, C. J. Pickard, M. C. Payne, *Phys. Rev. B* **1996b**, *54*, 16317.
[10] V. L. Deringer, A. L. Tchougréeff, R. Dronskowski, *J. Phys. Chem. A* **2011**, *115*, 5461.
[11] S. Maintz, V. L. Deringer, A. L. Tchougréeff, R. Dronskowski, *J. Comput. Chem.* **2013**, *34*, 2557.
[12] S. Maintz, V. L. Deringer, A. L. Tchougréeff, R. Dronskowski, *J. Comput. Chem.* **2016**, *37*, 1030.
[13] S. Maintz, M. Esser, R. Dronskowski, *Acta Phys. Polonica B* **2016b**, *47*, 1165.
[14] P. E. Blöchl, *Phys. Rev. B* **1994**, *50*, 17953.
[15] D. R. Hamann, M. Schlüter, C. Chiang, *Phys. Rev. Lett.* **1979**, *43*, 1494.
[16] G. B. Bachelet, D. R. Hamann, M. Schlüter, *Phys. Rev. B* **1982**, *26*, 4199.
[17] G. Kresse, J. Hafner, R. J. Needs, *J. Phys.: Condens. Matter* **1992**, *4*, 7451.
[18] H. W. Yeom, S. Takeda, E. Rotenberg, I. Matsuda, K. Horikoshi, J. Schaefer, C. M. Lee, S. D. Kevan, T. Ohta, T. Nagao, S. Hasegawa, *Phys. Rev. Lett.* **1999**, *82*, 4898.
[19] C. Gonzalez, F. Flores, J. Ortega, *Phys. Rev. Lett* **2006**, *96*, 136101.
[20] S. Wippermann, W. G. Schmidt, *Phys. Rev. Lett.* **2010**, *105*, 126102.
[21] E. Jeckelmann, S. Sanna, W. G. Schmidt, E. Speiser, N. Esser, *Phys Rev. B* **2016**, *93*, 241407.
[22] S.-W. Kim, J.-H. Cho, *Phys. Rev. B* **2016**, *93*, 241408.
[23] S. Wall, B. Krenzer, S. Wippermann, S. Sanna, F. Klasing, A. Hanisch-Blicharski, M. Kammler, W. G. Schmidt, M. Horn-von Hoegen, *Phys. Rev. Lett.* **2012**, *109*, 186101.
[24] T. Frigge, S. Wall, B. Krenzer, S. Wippermann, S. Sanna, F. Klasing, A. Hanisch-Blicharski, M. Kammler, W. G. Schmidt, M. Horn-*von Hoegen, Phys. Rev. Lett.* **2013**, *111*, 149602.
[25] T. Frigge, B. Hafke, T. Witte, B. Krenzer, C. Streubhr, A. Samad Syed, V. Miki Trontl, I. Avigo, P. Zhou, M. Ligges, D. von der Linde, U. Bovensiepen, M. Horn-von Hoegen, S. Wippermann, A. Lücke, S. Sanna, U. Gerstmann, W. G. Schmidt, *Nature* **2017**, 544, 207.
[26] F. Bloch, Z. Physik, *Z. Phys.* **1929**, *52*, 555.
[27] P. E. Blöchl, O. Jepsen, O. K. Andersen, *Phys. Rev. B* **1994**, *49*, 16223.
[28] L. A. Agapito, A. Ferretti, A. Calzolari, S. Curtarolo, M. Buongiorno Nardelli, *Phys. Rev. B* **2013**, *88*, 165127.
[29] P. Giannozzi, S. Baroni, N. Bonini, M. Calandra, R. Car, C. Cavazzoni, D. Ceresoli, G. L. Chiarotti, M. Cococcioni, I. Dabo, A. Dal Corso, S. de Gironcoli, S. Fabris, G. Fratesi, R. Gebauer, U. Gerstmann, C. Gougoussis, A. Kokalj, M. Lazzeri, L. Martin-Samos, N. Marzari, F. Mauri, R. Mazzarello, S. Paolini, A. Pasquarello, L. Paulatto, C. Sbraccia, S. Scandolo, G. Sclauzero, A. P. Seitsonen, A. Smogunov, P. Umari, R. M. Wentzcovitch, *J. Phys.: Condens. Matter* **2009**, *21*, 395502.
[30] P.-O. Löwdin, *J. Chem. Phys.* **1950**, *18*, 365.
[31] P. C. Pattnaik, J. L. Fry, N. E. Brener, G. Fletcher, *Int. J. Quantum Chem.* **1981**, *20*, 499.
[32] J. Perdew, K. Burke, M. Ernzerhof, *Phys. Rev. Lett.* **1996**, *77*, 3865.
[33] J. Perdew, K. Burke, M. Ernzerhof, *Phys. Rev. Lett.* **1997**, *78*, 1396.
[34] J. Nakamura, S. Watanabe, M. Aono, *Phys. Rev. B* **2001**, *63*, 193307.
[35] J.-H. Cho, D.-H. Oh, K. S. Kim, L. Kleinman, *Phys. Rev. B* **2001**, *64*, 235302.
[36] J.-H. Cho, J.-Y. Lee, L. Kleinman, *Phys. Rev. B* **2005**, *71*, 081310(R).
[37] S.-F. Tsay, *Phys. Rev. B* **2005**, *71*, 035207.
[38] W. G. Schmidt, M. Babilon, C. Thierfelder, S. Sanna, S. Wippermann, *Phys. Rev. B* **2011**, *84*, 115416.
[39] U. Gerstmann, N. J. Vollmers, A. Lücke, M. Babilon, W. G. Schmidt, *Phys. Rev. B* **2014**, *89*, 165431.
[40] H. Shim, G. Lee, J.-M. Hyun, H. Kim, *New J. Phys.* **2015**, *17*, 093026.
[41] F. Edler, I. Miccoli, S. Demuth, H. Pfnür, S. Wippermann, A. Lücke, W. G. Schmidt, C. Tegenkamp, *Phys. Rev. B* **2015**, *92*, 085426.
[42] P. H. Dederichs, S. Blügel, R. Zeller, H. Akai, *Phys. Rev. Lett.* **1984**, *53*, 2512.
[43] W. Humphrey, A. Dalke, K. Schulten, *J. Mol. Graph.* **1996**, *14*, 33.

Received: 30 March 2017
Revised: 3 May 2017
Accepted: 20 June 2017
Published online on 18 July 2017